https://doi.org/10.5194/egusphere-2025-2373
Preprint. Discussion started: 8 September 2025

Experimental investigation of temperature-induced variations in the diffuse attenuation coefficient of young sea ice: depth and wavelength dependence

Yu Zhang[1,2,3], Zhantang Xu[1,4], Ping Zhu[2,3], Cong Liu[1], Yuezhong Yang[1], and Huizeng Liu[2,3]

[1]State Key Laboratory of Tropical Oceanography, South China Sea Institute of Oceanology, Chinese Academy of Sciences, Guangzhou, 510301, China
[2]Institute for Advanced Study & Tiandu-Shenzhen University Deep Space Exploration Joint Laboratory & Space Science Center, Shenzhen University, Shenzhen,·518060, China
[3]MNR Key Laboratory for Geo-Environmental Monitoring of Great Bay Area & Guangdong Key Laboratory of Urban Informatics & Shenzhen Key Laboratory of Spatial Smart Sensing and Services, Shenzhen University, Shenzhen, 518060, China
[4]Guangdong Key Laboratory of Ocean Remote Sensing, South China Sea Institute of Oceanology, Chinese Academy of Sciences, Guangzhou, 510301, China

Correspondence to: Zhantang Xu (xuzhantang@scsio.ac.cn) and Huizeng Liu (huizeng.liu@szu.edu.cn)

Abstract. The light attenuation properties of sea ice play a critical role in regulating the radiative energy budget and primary production in polar regions. Previous studies have shown that the diffuse attenuation coefficient of downwelling irradiance (K_d) of young, thin sea ice is sensitive to changes in ice temperature (T_{ice}). However, the depth- and wavelength-dependent behavior of K_d under changing T_{ice} conditions remains poorly understood. To address this gap, a comprehensive investigation was conducted using synchronized measurements of K_d and T_{ice} from a cold laboratory experiment, a freezer experiment, and field observations in Liaodong Bay. The underlying mechanisms were further explored by analyzing the evolutions of sea ice microstructures and inherent optical properties, supported by Mie scattering theory and freezing equilibrium principles. Results revealed a distinct depth dependence: a negative correlation between K_d and T_{ice} was found in 95.96% of surface-layer measurements, while a positive correlation occurred in 38.38% of bottom-layer measurements. The overall correlation between K_d and T_{ice} was weaker in bottom layers compared to surface layers. This contrasting behavior is attributed to depth-dependent changes in the relative volume fractions of air and brine, which in turn affect scattering properties. No consistent trend in the K_d–T_{ice} relationship was found across wavelengths; however, increased variability was occasionally observed in the 443–555 nm range. These findings enhance our understanding of the thermal sensitivity of light attenuation in sea ice and provide valuable insights for improving radiative transfer parameterizations in climate models and marine ecosystem simulations.

https://doi.org/10.5194/egusphere-2025-2373
Preprint. Discussion started: 8 September 2025

1 Introduction

In recent decades, the distribution of Arctic sea ice has declined at an average rate of 3% per decade, accompanied by a general thinning of ice and an increasing percentage of seasonal sea ice. These changes are driven by global warming, which in turn alters the energy balance in the polar ice region (Comiso et al., 2008; Marks et al., 2017; Nicolaus et al., 2012; Perovich and Polashenski, 2012). The optical properties of sea ice and their variations play a critical role in the radiative balance of ice-covered areas (Perovich, 2005; Graversen et al., 2008; Zhang et al., 2023). For example, the rise in atmospheric temperatures induces accelerated sea ice melt, which reduces surface albedo through the exposure of darker ocean surfaces (Perovich et al., 2011; Arndt and Nicolaus, 2014; Yu et al., 2024). This albedo decline allows more solar radiation to enter the ice, elevating ice temperatures and further accelerating the melting and recession of sea ice. Current estimates suggest 69% of incident solar radiation at Arctic air-sea interfaces undergoes ice surface reflection, while the remaining 31% penetrates the sea ice, with some reaching the underlying seawater (Ebert et al., 1995; Perovich, 2005; Perovich et al., 2020). Though the albedo feedback mechanism has been thoroughly characterized as a climate amplifier(Ingram et al., 1989; Curry et al., 1995; Hall, 2004), critical knowledge gaps persist regarding the transport and attenuation of solar radiation within the ice and its response to environmental changes.

Sea ice is not a homogeneous medium composed solely of ice crystals; instead, its structure is characterized by the irregular presence of air bubbles, brine inclusions, precipitated salts, and various inorganic and organic particles (Light et al., 2003a, 2004). The distribution of light within the upper ocean is closely linked to the microstructure of sea ice, which is crucial for its optical properties. Temperature, as a core thermodynamic factor, directly dominates key processes such as sea ice growth and ablation by regulating the energy balance and physical properties of sea ice, and is a key factor influencing the evolution of microstructure(Serreze et al., 2007; Zhang et al., 2023). Variations in ice temperature (T_{ice}) can alter the size, number, spatial distribution, and chemical properties of these microstructures, leading to changes in the inherent optical properties of sea ice, such as absorption and scattering properties. These alterations, in turn, affect the radiative transfer of solar radiation through the ice and modify its apparent optical properties (Light et al., 2003a, 2004; Yu et al., 2022; Yu et al., 2024). The diffuse attenuation coefficient of downwelling irradiance ($K_d(\lambda)$) is a key apparent optical property quantifying the attenuation of solar radiation within the ice column (Perovich, 2017). Its response to changes in T_{ice} can influence physical and biological processes regulated by radiation levels, including the primary production of ice algae and the dynamics of sea ice melt and growth (Perovich and Grenfell, 1981; Grenfell, 1983; Zhang et al., 2023).

Early studies generally concluded that temperature has a limited effect on the optical properties of sea ice, based on experimental observations (Erickson, 2002; Light et al., 2003a; Frantz et al., 2019) and theoretical simulations of radiative transfer (Grenfell, 1983; Light et al., 2004; Yu et al., 2024). Research on sea ice often overlooked the temperature response of $K_d(\lambda)$ in the context of radiative transfer within sea ice (Nicolaus et al., 2012; Perovich et al., 2020; Arndt and Nicolaus, 2014). However, recent studies have highlighted that the variability in the microstructure and optical properties of sea ice has become more pronounced due to the increasing proportion of high-salinity seasonal sea ice (Ehn et al., 2007; Light et al.,

https://doi.org/10.5194/egusphere-2025-2373
Preprint. Discussion started: 8 September 2025

2015; Taskjelle et al., 2016; Kauko et al., 2017; Thomas et al., 2021). This shift in ice composition may amplify the impact of environmental changes on radiative transfer through sea ice (Yu et al., 2024; Yu et al., 2022; Light et al., 2015; Grenfell et al., 2006; Wang et al., 2020). For instance, research has shown that microstructural changes in Arctic sea ice driven by climate warming could significantly alter the amount of solar radiation transmitted to the upper ocean, particularly in thin ice at the edge zones, even if the ice thickness remains unchanged (Yu et al., 2024). Additionally, a study has observed that change in T_{ice} can substantially affect the magnitude of K_d for young thin sea ice (Zhang et al., 2023). Nevertheless, the wavelength and depth dependencies in the variations of $K_d(\lambda)$ with T_{ice} remain to be fully investigated.

To address this gap, this study explores the variation in $K_d(\lambda)$ with T_{ice} across different ice layers and wavelengths, utilizing simultaneous observations of both $K_d(\lambda)$ and T_{ice} obtained from a cold laboratory, a freezer, and field measurements in Liaodong Bay, China. The factors driving the observed depth- and wavelength-dependent variations in $K_d(\lambda)$ were analyzed in terms of sea ice microstructure and bio-optical properties, employing Mie theory and freezing equilibrium theory.

2 Data and Method

2.1 Laboratory experiments

Laboratories offer a controlled environment where the growth and melting of sea ice can be manipulated and replicated, making them valuable for quantifying variations in $K_d(\lambda)$ in response to changes in T_{ice}. In this study, synchronous observations of downwelling irradiance ($E_d(\lambda)$) and T_{ice} profiles were conducted in two laboratory settings: a cold laboratory at the University of Manitoba, Canada, in 2016 (Fig. 1a), and a freezer at the South China Sea Institute of Oceanology, Chinese Academy of Sciences, in 2021 (Fig. 1b) (Zhang et al., 2023). In both experiments, multiple irradiance probes and thermometers were installed at different depths prior to freezing to monitor temperature and irradiance profiles. Continuous measurements of $E_d(\lambda)$ and T_{ice} commenced once the sea ice at the observed depth had fully formed.

In the cold laboratory experiment, three standard-size irradiance probes were placed at depths of 3.45 cm, 9.5 cm, and 16.8 cm within the sea ice. A S2000 spectrometer (Ocean Optics, Inc., USA) and hyperspectral cosine irradiance sensors (RAMSES-ACC-VIS, Trios, Inc., Germany) were utilized to measure $E_d(\lambda)$ over 40 days, with spectral and temporal resolutions of 3.3 nm and 5 minutes, respectively, across a wavelength range of 320 nm to 950 nm. The $K_d(\lambda)$ were calculated from the $E_d(\lambda)$ between these depth intervals. Specifically, $K_{d12}(\lambda)$, $K_{d23}(\lambda)$ and $K_{d13}(\lambda)$ represent values derived from $E_d(\lambda)$ over the intervals of 3.45–9.5 cm, 9.5–16.8 cm, and 3.45–16.8 cm, respectively.

In the freezer experiment, four miniature irradiance probes were installed at depths of 10.9 cm, 14 cm, 17 cm, and 21.8 cm (Fig. 1c). Three Maya 2000 spectrometers (Ocean Optics, Inc., USA) were employed to measure $E_d(\lambda)$ profiles for 24 days, with spectral and temporal resolutions of approximately 0.5 nm and 1-3 hours, respectively. In this experiment, $K_{d12}(\lambda)$, $K_{d24}(\lambda)$ and $K_{d14}(\lambda)$ were derived from $E_d(\lambda)$ over the intervals of 10.9–14 cm, 17–21.8 cm, and 10.9–21.8 cm, respectively.

https://doi.org/10.5194/egusphere-2025-2373
Preprint. Discussion started: 8 September 2025

In both experiments, LED lights powered by low-voltage direct current served as light sources: sixty-watt LEDs in the cold laboratory and 100-watt LEDs in the freezer. The radiant intensity fluctuations for both light sources were maintained at less than 5%(Zhang et al., 2023), which meets general stability standards for artificial light sources (Zhao et al., 2010). In the cold laboratory experiment, a 'T'-type thermocouple array was used to measure T_{ice} profiles with a depth resolution of 2 cm, while in the freezer experiment, four electronic thermometers measured the T_{ice} of the ice layers between each pair of adjacent irradiance probes.

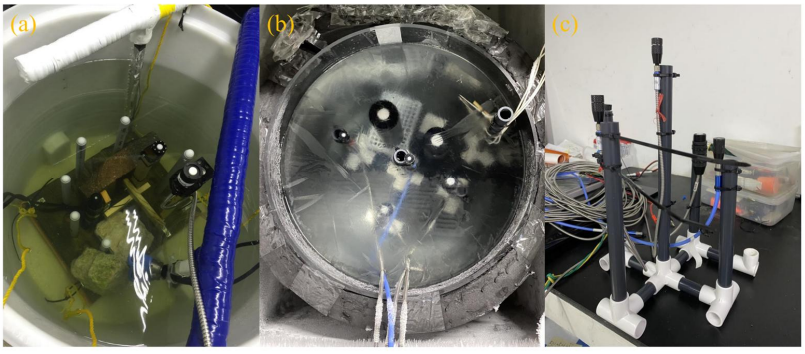

Figure 1. Images of (a) cold laboratory experiment, (b) freezer experiment, and (c) probe bracket used in the freezer experiment.

2.2 Field validation in Liaodong Bay

Liaodong Bay, situated at the northernmost part of the Bohai Sea, is the lowest-latitude sea-ice-covered area in the Northern Hemisphere. Its ice-freezing period typically extends from December to February. The substantial diurnal variation in air temperature in Liaodong Bay, which can exceed 15 °C (Xu et al., 2012b; Zhang et al., 2023), provides a natural environment for observing variations in $K_d(\lambda)$ in response to changes in T_{ice}. The sea ice in Liaodong Bay is classified as seasonal sea ice. Although most of the ice in this region consists of floating ice, the study focused on leveled, shoreline-fixed ice to ensure the safety of field researchers (Fig. 2). For this type of sea ice, the T_{ice} of the upper layer is primarily influenced by air temperature, while the T_{ice} of the lower layer is regulated by water temperature (Xu et al., 2012b).

One validation experiment was conducted in Liaodong Bay from January 6 to 17, 2022. In this experiment, artificial holes with diameters exceeding 1 m were drilled into the sea ice to accommodate optical probes. Maya 2000 spectrometers were employed in both experiments, maintaining the same spectral and temporal resolutions as those used in the freezer experiment. The probes were installed at depths of 4 cm, 10 cm, 15 cm, 23 cm, and 32 cm, fixed using type-'L' brackets. $K_{d12}(\lambda)$, $K_{d23}(\lambda)$ and $K_{d13}(\lambda)$ were derived from $E_d(\lambda)$ over the intervals of 4–10 cm, 10–15 cm, and 4–15 cm, respectively. The $E_d(\lambda)$ data from the last two probes were both excluded from the analysis, as the corresponding depth was not fully frozen.

https://doi.org/10.5194/egusphere-2025-2373
Preprint. Discussion started: 8 September 2025

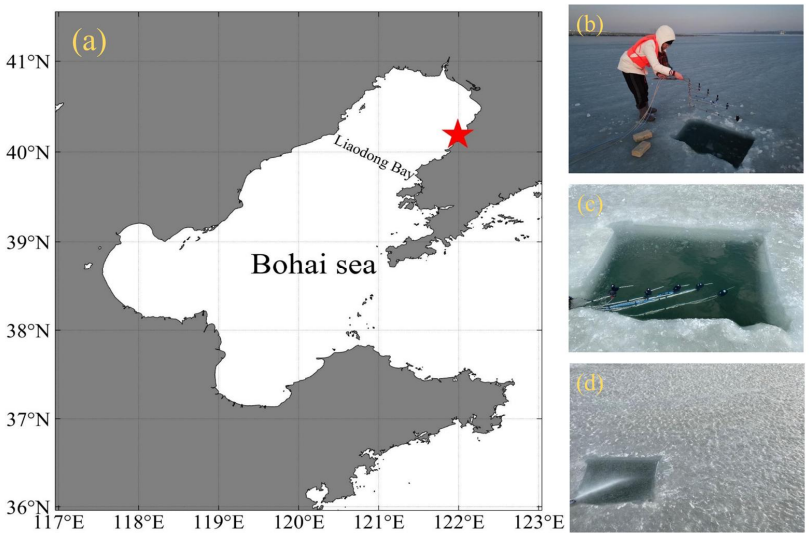

Figure 2. (a) Location of the study area in Liaodong Bay and images of (b) placing optical probes, (c) the unfrozen observation point, and (d) the frozen observation point.

2.3 Acquisitions of physical and bio-optical properties

2.3.1 Measurement of salinity and density

The physical properties of sea ice were obtained using standard ice coring and stratified techniques. Ice cores were sectioned vertically into layers approximately 5 cm thick to determine salinity and density. Due to the inherently heterogeneous nature of sea ice, both vertical and horizontal variations in its physical properties are significant. However, for the purpose of this study, ice samples with lateral dimensions less than 50 cm were assumed to be horizontally homogeneous. The stratified ice samples were transported to a laboratory maintained at approximately 5 °C and melted completely. The salinity of the meltwater was measured using a conductivity salinometer.

The density of sea ice was determined via the gravimetric volume method. Each sample was machined into a cuboid with dimensions of 10 cm × 10 cm × 5 cm. The mass (m_i) was measured using a balance with a precision of 0.1 g, and the volume (V_i) was determined using an electronic vernier caliper with a resolution of 0.01 mm. The density (ρ_i) was then calculated as:

$$\rho_i = \frac{m_{\text{ice}}}{V_i}, \quad (1)$$

2.3.2 Measurement of microstructure

The microstructure of sea ice was analyzed using a Fahrenheit cold table and a high-resolution digital camera. Ice samples were first cut into 5 cm × 5 cm cubes and placed onto a glass plate maintained just above 0°C. After several minutes, the

https://doi.org/10.5194/egusphere-2025-2373
Preprint. Discussion started: 8 September 2025

cubes adhered to the surface as the melt refroze. Each adhered sample was then sliced into thin sections (thickness < 1 mm) using a paring knife.

The thin sections were observed under both polarized and natural light and photographed to document their internal structures. A straightedge was placed adjacent to each section during imaging to provide a spatial reference. The number and cross-sectional area of air bubbles and brine inclusions were quantified using the ImageJ image analysis software.

2.3.3 Calculation of absorption coefficient

The absorption properties of sea ice were determined using traditional ice core sampling. Each core was divided into several 5 cm-thick sections, which were subsequently melted at approximately 5 °C. Between 50–200 mL of the meltwater was filtered through 25-mm Whatman GF/F glass fiber filters under low vacuum conditions. The filters were then scanned using a spectrophotometer (PerkinElmer Lambda 650S, Waltham, MA, USA) to determine the total particulate absorption coefficient ($a_p(\lambda)$).

The total absorption coefficient of sea ice, $a_{total}(\lambda)$, was calculated following the approach described in (Zhang et al., 2023):

$$a_{total}(\lambda) = a_{ice}(\lambda)V_{ice}+a_{brine}(\lambda)V_{brine}+a_p(\lambda)+a_{CDOM}(\lambda)\ , \quad (2)$$

Here, $a_{ice}(\lambda)$ and $a_{brine}(\lambda)$ represent the absorption coefficients of pure ice and brine, respectively. These parameters were derived from the measurements of bubble-free sea ice by Grenfell and Perovich (1981), and seawater in the Arctic Ocean by Smith and Baker (1981). The volume fractions V_{ice} and V_{brine} were estimated using the temperature-, salinity-, and density-based empirical relationships proposed by Cox and Weeks (1983).

2.3.4 Calculation of scattering coefficient

The scattering coefficient was estimated based on the equivalent sphere approximation, which assumes that air bubbles and brine inclusions can be modeled as spheres while preserving their total volume and surface area. The equivalent cross-sectional area (ψ) for the inclusions was calculated as:

$$\psi = \int_{r_{min}}^{r_{max}} \pi r_{eq}^2 N(r_{eq}) dr_{eq}, \quad (3)$$

where r_{eq} is the equivalent spherical radius, and $N(r_{eq})$ is the number density of spheres (Light et al., 2003a, 2004). Assuming that all inclusions are uniformly distributed and isolated, $N(r_{eq})$ was approximated as:

$$N(r_{eq}) = \frac{1}{0.05*0.05*l}, \quad (4)$$

where l is the average vertical length of the inclusions. The radius r_{eq} was derived from the measured cross-sectional area (S_h) in the horizontal plane:

$$r_{eq} = \sqrt{\frac{S_h}{\pi}}, \quad (5)$$

The scattering coefficient (σ) was then calculated as:

https://doi.org/10.5194/egusphere-2025-2373
Preprint. Discussion started: 8 September 2025

$$\sigma = \int_{r_{min}}^{r_{max}} Q_{sca} \pi r_{eq}^2 N(r_{eq}) dr_{eq} \quad (6)$$

where Q_{sca} is the scattering efficiency, which was approximated as 2. This simplification is valid under the assumption that the inclusions are significantly larger than the wavelength of visible light, as supported by previous studies (Light et al., 2004).

3 Results

3.1 Optical and physical properties of experimental sea ice

The vertical profiles of the $K_d(\lambda)$ for different ice layers in the cold laboratory, freezer, and Liaodong Bay experiment are shown in Fig. 3. In the artificially grown sea ice from the laboratory experiments, the surface ice layers consistently exhibited higher K_d values than the deeper layers. Specifically, the $K_d(\lambda)$ of the surface layers ($K_{d12}(\lambda)$) was greater than that of the bottom layers ($K_{d23}(\lambda)$) in the cold laboratory experiment, and $K_{d12}(\lambda)$ was greater than $K_{d24}(\lambda)$ in the freezer experiment (Fig. 3a and 3b). In the freezer experiment, $K_d(\lambda)$ for the middle ice layer were not reported due to anomalous measurements: the $E_d(\lambda)$ in the third layer was unexpectedly higher than in the second layer, despite the absence of instrument malfunction. Similar phenomena have been reported in previous studies (Pegau and Zaneveld, 2000; Ehn et al., 2008; Xu et al., 2012a), although the underlying causes remain unclear. In contrast, natural sea ice from Liaodong Bay exhibited an inverse vertical pattern, with the bottom layer showing a greater $K_d(\lambda)$ than the surface layer ($K_{d23}(\lambda) > K_{d12}(\lambda)$, Fig. 3c).

The spectral behavior of $K_d(\lambda)$ displayed typical patterns across experiments. In the cold laboratory experiment, $K_d(\lambda)$ decreased monotonically with increasing wavelength (Fig. 3a). In the freezer experiment, $K_d(\lambda)$ had a small peak around 440 nm. For the Liaodong Bay sea ice, $K_d(\lambda)$ followed an exponential decay within the 430–580 nm range, and exhibited a slight increase at wavelengths beyond 580 nm. Spectrometer measurements below 430 nm exhibited significant noise and were therefore excluded from both the figures and the subsequent analysis.

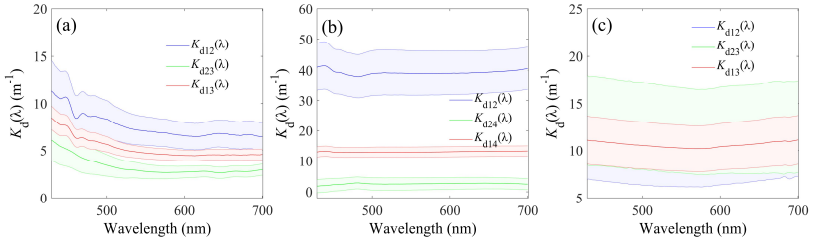

Figure 3. $K_d(\lambda)$ of different ice layers for (a) cold laboratory experiment, (b) freezer experiment, and (c) Liaodong Bay experiment.

https://doi.org/10.5194/egusphere-2025-2373
Preprint. Discussion started: 8 September 2025

Apart from T_{ice}, the physical properties of sea ice were only measured during the Liaodong Bay experiment. Fig 4a presents the average T_{ice} profile recorded in 2022, with all values exceeding −5°C and showing a slight increase with increasing ice thickness. During the field temperature experiment, Liaodong Bay experienced a warming phase, with T_{ice} ranging from −6.6°C to −1.2°C. The salinity profile exhibited a typical "C"-shaped pattern, with higher salinity values predominantly observed in the bottom layers (Fig. 4b). Similarly, higher density was generally found in the middle and bottom layers (Fig. 4c), likely due to increased brine content in these layers.

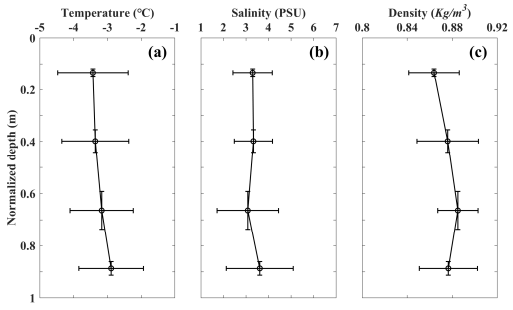

Figure 4. Average profiles of (a) temperature, (b) salinity, and (c) density for Liaodong Bay sea ice measured in 2022.

3.2 Variations of $K_d(\lambda)$ with T_{ice} in the cold laboratory experiment

Fig. 5a illustrates the temporal evolutions of the vertically averaged $K_d(555)$ for different ice layers—namely, $K_{d12}(\lambda)$, $K_{d23}(\lambda)$, and $K_{d13}(\lambda)$—under the cold laboratory experiment. The results show that once sea ice formed (indicated by a stable T_{ice} < -2 °C), $K_d(555)$ mostly decreased with increasing T_{ice}, and increased as T_{ice} decreased. Regression and quantitative analyses reveal significant differences in the influences of temperature changes on K_d of different layers. Fig. 5b-5g depict the spectral patterns of the correlation coefficient (R) between $K_d(\lambda)$ at wavelengths of 443, 469, 488, 531, 547, 555, 645, 667, and 678 nm and the corresponding T_{ice} during six distinct temperature variation phases. Over 92% of $K_{d12}(\lambda)$ showed a negative correlation with T_{ice}, with R of typically below zero. The mean R between $K_{d12}(\lambda)$ and T_{ice} at the respective wavelengths were -0.48, -0.50, -0.50, -0.50, -0.48, -0.48, -0.42, -0.42 and -0.43, with p-values <0.01. For $K_{d23}(\lambda)$, although most correlations with T_{ice} were also negative, the overall relationship was weaker than that observed for $K_{d12}(\lambda)$. The mean R values ranged from -0.08 to -0.26 across the wavelengths examined, with p-values <0.05, except that at 488 nm and 547 nm. In contrast, $K_{d13}(\lambda)$exhibited consistently negative correlations with T_{ice}, with mean R values ranged from –0.55 to –0.66, with p-values <0.001. The magnitudes of their linear regression were intermediate between those of $K_{d12}(\lambda)$ and $K_{d23}(\lambda)$.

https://doi.org/10.5194/egusphere-2025-2373
Preprint. Discussion started: 8 September 2025

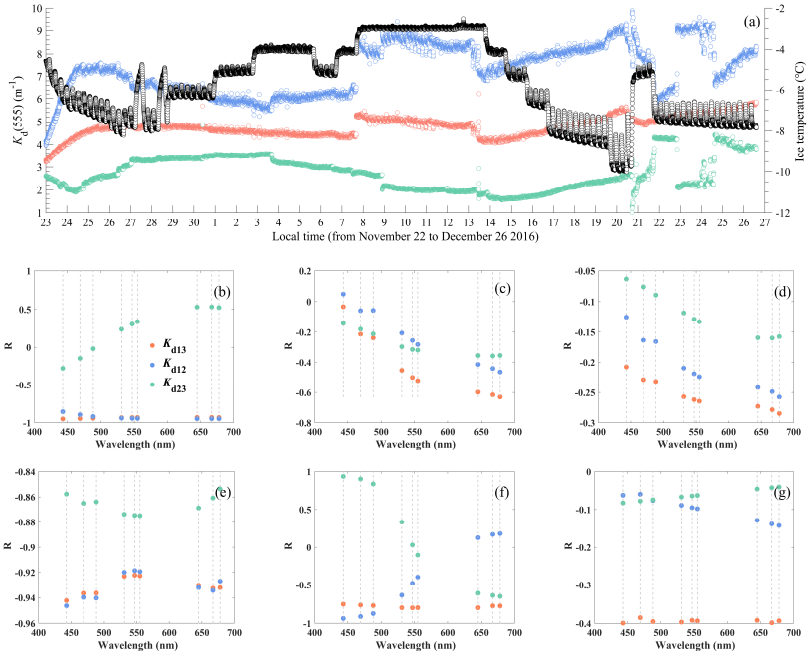

Figure 5. (a) Temporal evolutions of the K_{d13}(555), K_{d12}(555) and K_{d23}(555), and (b)-(g) slopes of linear regressions between T_{ice} and K_d of different depth range at 443, 469, 488, 531, 547, 555, 645, 667 and 678 nm for six different temperature change processes in the cold laboratory experiment. The legend in (b) are applicable to all sub-figures.

Nevertheless, positive correlations were observed in certain cases for both $K_{d12}(\lambda)$ and $K_{d23}(\lambda)$. For example, during the first warming phase (Fig. 5c), $K_{d12}(443)$ exhibited a positive correlation with T_{ice} (R = 0.05, p-value < 0.01), while in the second warming phase (Fig. 5f), K_{d12} at 645, 667, and 678 nm also showed positive correlations (R = 0.13, 0.17 and 0.18; all with p-value < 0.05). Additionally, during the first cooling phase (Fig. 5b), $K_{d23}(\lambda)$ from 531 to 678 nm showed significant positive correlations with T_{ice}, with R values ranging from 0.24 to 0.52 (p-value < 0.01).

The variations of $K_d(\lambda)$ with T_{ice} exhibited more complexity from the perspective of varying wavelength. The spectral patterns of the R varied across temperature variation phases. For instance, during the first cooling phase (Fig. 5a), R for both K_{d12} and K_{d13} remained nearly constant across wavelengths, while R for K_{d23} increased from negative to positive with increasing wavelength. During the last cooling phase, R remained relatively stable across the spectrum. However, for the remaining four warming and cooling processes, R varied considerably with wavelength. No clear pattern emerged in the wavelength dependence of $K_d(\lambda)$ variation with T_{ice}. But overall, K_{d12} and K_{d23} showed more significant dependence on wavelength compared to K_{d13}. It is worth noting that the results for 412 nm are not shown here due to the multiple instances of negative $K_d(412)$ observed in the cold laboratory experiment.

https://doi.org/10.5194/egusphere-2025-2373
Preprint. Discussion started: 8 September 2025

3.3 Variations of $K_d(\lambda)$ with T_{ice} in the freezer experiment

The temporal evolution of the vertically averaged $K_d(555)$ for different ice layers—$K_{d12}(\lambda)$, $K_{d24}(\lambda)$, and $K_{d14}(\lambda)$—were also examined under the freezer experiment to characterize the overall variation of K_d with T_{ice} (Fig. 6a). The results closely aligned with those obtained in the cold laboratory experiment. Overall, $K_d(555)$ exhibited a decreasing trend with increasing T_{ice} and an increasing trend with decreasing T_{ice}, with some exceptions in the second warming phase, where K_d first decreased and then increased with increasing T_{ice}. This relationship was most clearly observed in the temporal evolution of $K_{d12}(\lambda)$.

To further quantify these relationships, linear regression analyses were conducted between T_{ice} and K_d (K_{d12}, K_{d24}, and K_{d14}) at wavelengths of 443, 469, 488, 531, 547, 555, 645, 667, and 678 nm. Fig. 6b-6e present the corresponding R across two cooling and two warming phases. Specifically, the mean R values for the four temperature variation phases were -0.97, -0.88, -0.96 and -0.51 for K_{d12} (with p-values <0.001 for the first three phases and <0.05 for the fourth), and -0.23, 0.49, 0.93 and 0.84 for K_{d24} (with p-values >0.05 for the first phase and <0.01 for the remaining three), and -0.93, -0.79, -0.67 and 0.13 for K_{d14} (with p-values <0.001 for the first three and >0.05 for the last phase). Among the three layers, the influence of T_{ice} on $K_{d12}(\lambda)$ was the most pronounced. Notably, K_{d24} exhibited trends opposite to those of K_{d12} with respect to T_{ice}.

In particular, the correlation between K_d and T_{ice} showed minimal spectral dependence across the examined wavelengths and remained relatively consistent for each layer, except that for K_{d24} in the first cooling phase, with R value decreasing with increasing wavelengths (Fig. 6b). This is significantly different from that observed in the cold laboratory experiment. It is noted that the $K_d(555)$ for the ice layer between the third and fourth probes were excluded from the analysis due to anomalous measurements: the observed $E_d(\lambda)$ at the third probe was consistently lower than that at the fourth probe, which is hard to account for.

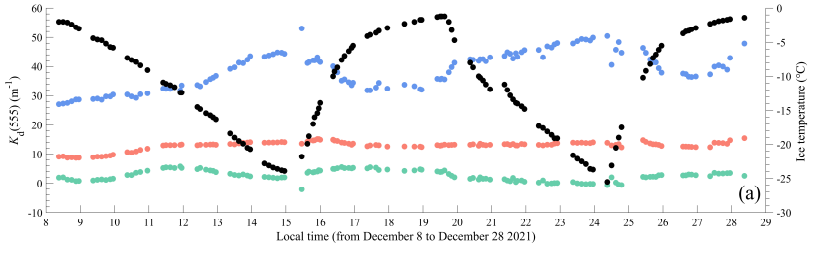

https://doi.org/10.5194/egusphere-2025-2373
Preprint. Discussion started: 8 September 2025

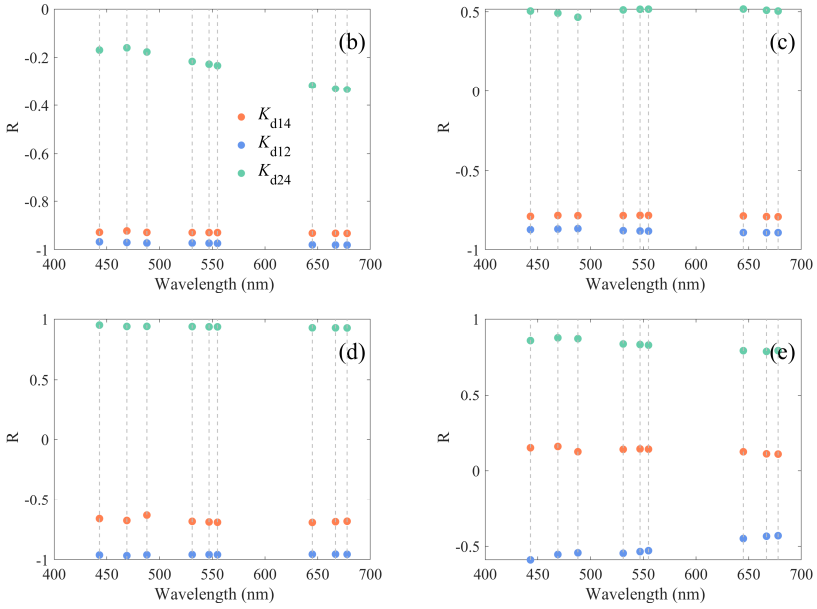

Figure 6. (a) Temporal evolutions of the K_{d14}(555), K_{d12}(555) and K_{d24}(555), R values of linear regressions between T_{ice} and K_d of different depth ranges at the center wavelength of MODIS in the freezer experiment: (b) cooling (-2~-9.1), (c) cooling (-10.9~-23.9), (d) warming (-25.1~-8.7), and (e) warming (-8.7~-1.2). The legend in (b) are applicable to all sub-figures.

3.4 Variations of $K_d(\lambda)$ with T_{ice} in the Liaodong Bay experiments

Fig. 7 present the R values from linear regression analyses between T_{ice} and $K_d(\lambda)$ for different ice layers observed during the 2022 Liaodong Bay experiment. These analyses correspond to a general warming phase from January 11 to 17, 2022, during which T_{ice} ranged from -6.6 ℃ to -1.2 ℃ and exhibited daily fluctuations. Unlike the results from cold laboratory and freezer experiments, the influence of T_{ice} on $K_d(\lambda)$ was relatively consistent across different ice layers in the field. For example, $K_{d12}(\lambda)$ was negatively correlated with T_{ice} during the observation period, with a mean R value of -0.40 (mean p-value <0.05). Similarly, $K_{d23}(\lambda)$ also showed a statistically significant negative correlation with T_{ice} (mean R = -0.39, p-value < 0.05). Additionally, the correlation between K_{d12} and T_{ice} exhibited minimal spectral dependence across the examined wavelengths and remained relatively consistent. In contrast, K_{d23} exhibited pronounced spectral variability: the R values for its correlations with T_{ice}decreased from 443 nm to 555 nm and then increased toward 678 nm.

https://doi.org/10.5194/egusphere-2025-2373
Preprint. Discussion started: 8 September 2025

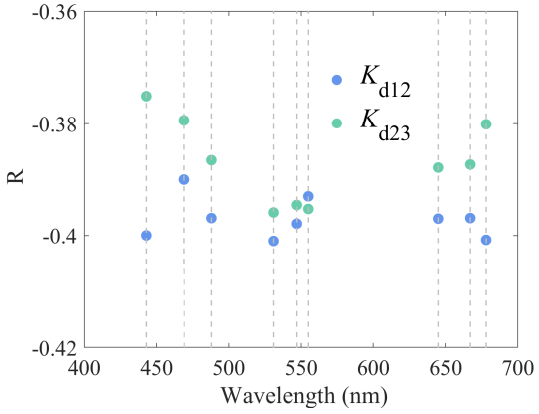

Figure 7. *R* values of linear regressions between T_{ice} and K_d of different depth ranges at the center wavelength of MODIS in the 2022 Liaodong Bay experiments.

4. Discussion

4.1 Depth-dependent variations in $K_d(\lambda)$ with T_{ice} from the perspective of microstructure

The variations in $K_d(\lambda)$ across different ice layers exhibited contrasting trends with respect to T_{ice} in some cases (Figs. 5-6). Specially, surface layers typically showed negative correlations between $K_d(\lambda)$ and T_{ice}, while positive correlations were more often observed in the bottom ice layers. To explore the underlying causes of these depth-dependent patterns, we analyzed the number and size of air bubbles and brine inclusions in ice samples. Statistical summaries revealed that the upper layers contained a greater number of inclusions compared to the lower layers (Fig. 8a). At depths of 0, 5, 10, 15, and 20 cm, the total counts of air and brine inclusions were 558, 285, 233, 82, and 98, respectively, with corresponding area fractions of 3.63%, 2.24%, 2.74%, 1.61%, and 1.38%.

To further investigate the depth-dependent variation of $K_d(\lambda)$, the V_{brine} and V_{air} were quantified in three artificially partitioned layers: a 5-cm thick surface layer, a 10-cm thick middle layer, and a 5-cm thick bottom layer. These values were estimated from measurements of T_{ice}, salinity, and density. The results indicated that V_{air} decreased with depth, while V_{brine} increased. Specially, the average V_{air} values in the surface, middle, and bottom layers were 8.04%, 6.09%, and 5.02%, respectively, whereas the corresponding average V_{brine} were 4.46%, 4.41%, and 5.75%. Furthermore, both V_{brine} and V_{air} tended to increase with rising T_{ice} (Fig. 8b and 8c). For example, V_{air} increased from 4.72% to 10.72% in the surface layer, 3.33% to 9.93% in the middle layer, and 2.95% to 9.44% in the bottom layer. Although the magnitude of V_{air} changes was similar across layers, the surface layer exhibited the greatest variability. (Fig. 8b). In contrast, the largest changes in V_{brine} occurred in the bottom layer, increasing from 2.78% to 6.83%, 3.18% to 6.53%, and 2.54% to 9.44% in the surface, middle,

https://doi.org/10.5194/egusphere-2025-2373
Preprint. Discussion started: 8 September 2025

and bottom layers, respectively. These differences in the variation patterns of V_{air} and V_{brine} among layers are likely key drivers of the observed depth-dependent characteristics of $K_d(\lambda)$–T_{ice} relationships.

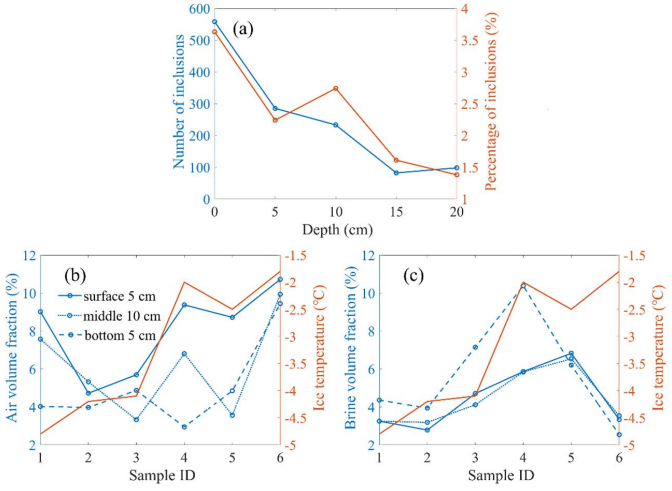

Figure 8. Variations of V_{air} and V_{brine} with T_{ice} at different depths of layers. It should be noted that the samples were arranged in the order of increasing T_{ice} to better present the pattern of change.

The pronounced variation in V_{air} observed in the surface layer coincided with a smaller V_{brine} (Fig. 9), a pattern likely linked to brine drainage induced by the absorption of shortwave radiation. As solar energy is absorbed, it promotes melting along grain boundaries, enhancing ice porosity and possibly triggering flushing or similar processes (Macfarlane et al., 2023). The increase in V_{air} contributes to the rise in K_d, thereby explaining the observed negative correlation between K_d and T_{ice} in the surface ice layer of Liaodong Bay. This process is driven by increased solar radiation during warmer periods, which elevates both T_{ice} and V_{air}, thereby influencing $K_d(\lambda)$. In contrast, laboratory experiments were conducted under artificial lighting with minimal fluctuations in shortwave radiation. In the freezer experiment, the light intensity variation was limited to an average of 4.3% over intervals shorter than one hour. In the cold laboratory experiment, over 80% of recorded fluctuations were less than 3% (Zhang et al., 2023). This stable lighting environment was insufficient to significantly alter V_{air}, suggesting that the negative correlation between K_d and T_{ice} observed in laboratory surface ice primarily reflects thermal rather than radiative effects.

https://doi.org/10.5194/egusphere-2025-2373
Preprint. Discussion started: 8 September 2025

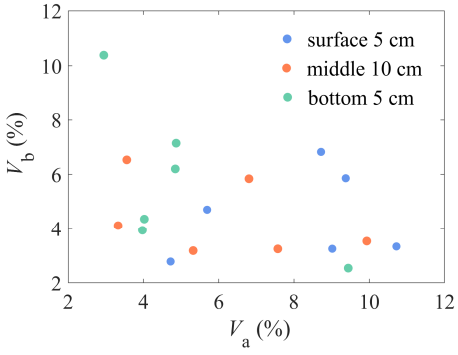

Figure 9. Relationships between V_{air} and V_{brine} for the surface, middle and bottom layers, respectively.

In the bottom layer, changes in V_{air} with T_{ice} were minimal, while V_{brine} exhibited the most significant variation (Fig. 9). This layer contained the highest V_{brine} and inclusion counts, resulting in extensive brine–crystal boundary interfaces. These interfaces promote melting along grain boundaries during warming (Macfarlane et al., 2023; Dash et al., 2006). Unlike the surface, the bottom layer is submerged and maintains a relatively low V_{air}, limiting the influence of flushing. Consequently, changes in V_{air} in this layer are largely attributed to thermal effects on V_{brine}. As brine inclusions melt, both V_{brine} and V_{air} increase due to the higher density of brine relative to ice (Light et al., 2003a). The formation of new air bubbles—referred to as "active bubbles" —results from melting around brine inclusions. Their development is governed by changes in V_{brine}, due to the requirement for air-brine equilibrium in sea ice (Crabeck et al., 2019; Light et al., 2003a). The newly formed air bubbles may subsequently migrate upward.

The middle layer exhibited intermediate changes in V_{air} and V_{brine}, with trends more similar to those in the surface layer (Fig. 9). This may be related to reduced freeboard during flood tide sampling. Two samples from this layer showed V_{brine}/V_{air} ratios more akin to those in the bottom layer, possibly reflecting limited internal connectivity within the ice matrix. Variations in the middle layer were more complex and less predictable, influenced by both melt progression and surrounding hydrodynamic conditions. Additionally, the vertical stratification of ice is influenced by its crystalline structure, which in Liaodong Bay transitions from granular ice near the surface to columnar ice at depth (Xu et al., 2012b). This structural change also affects the spatial distribution of air bubbles, as the geometries of granular and columnar ice dictate different patterns of air inclusion arrangement.

In summary, the variations in $K_d(\lambda)$ with T_{ice} are primarily driven by changes in V_{air} in the upper ice layer, and by changes in V_{brine} in the lower layer. This distinction highlights the differing roles of air and brine inclusions, with upper-layer K_d variations dominated by air bubble dynamics, while lower-layer responses are more sensitive to brine inclusions.

https://doi.org/10.5194/egusphere-2025-2373
Preprint. Discussion started: 8 September 2025

4.2 Depth-dependent variations in $K_d(\lambda)$ with T_{ice} from the perspective of IOPs

To investigate the influence of V_{air} and V_{brine} on sea ice optical properties, the scattering coefficient of different ice layers were calculated using Mie theory, based on in situ microstructural measurements. Fig. 10 illustrates the variation in σ across four depth intervals: 0-5 cm, 5-10 cm, 10-15 cm, and 15-20 cm. Results show that the uppermost layer exhibits higher σ values compared to the deeper layers, primarily due to its higher air bubble content.

Although the trend in σ with T_{ice} was consistent across all layers, the relationships between K_d and T_{ice} vary with depth. Given that the K_d is more sensitive to backscattering than to total scattering, further analysis focused on the variations in scattering direction. According to the "similarity principle" for highly scattering media, K_d should remain consistent if the similarity parameters (S) remains unchanged (Light et al., 2003b, 2004). The parameter S is approximated as: $S = \sigma(1\text{-}g)$, where g is the asymmetry parameter representing the the mean cosine of the scattering angle (Van De Hulst, 1980). Based on the freezing equilibrium model and the equivalent sphere theory, an increase in T_{ice} leads to a higher inclusion aspect ratio (ψ), thereby increasing σ. In the surface layer, the observed negative correlation between K_d and T_{ice} implies that both σ and g increase with T_{ice}, with the increase in g playing a more dominant role in reducing S and decreasing K_d. This indicates that, in the upper ice layer, changes in scattering direction induced by air bubbles are more influential than changes in scattering magnitude.

In contrast, the positive correlation between K_d and T_{ice} in the bottom layer suggests that σ due to brine inclusions is the dominant factor. However, when brine inclusions start to merge, their ψ decreases, leading to a reduction in σ. This mechanism may explain the frequently observed shift to a negative K_d-T_{ice} relationship in the deeper layers. For instance, in the cold laboratory experiment, K_{d23} at specified wavelengths showed a negative correlation with T_{ice} during the first warming phase (Fig. 5b). Additionally, change in K_d with T_{ice} in deeper layers tend to be less pronounced, as evidenced by flatter regression slopes and larger p-values (> 0.05). This muted response may result from attenuation of thermal signals as they propagate downward through the ice column.

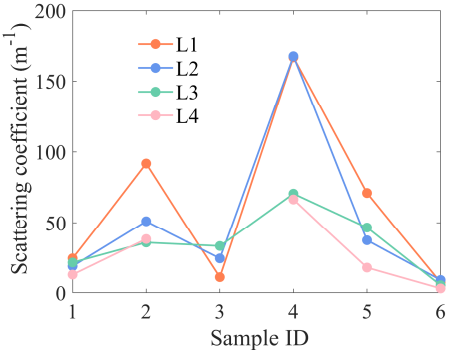

Figure 10. σ of layers with different ranges of depths.

https://doi.org/10.5194/egusphere-2025-2373
Preprint. Discussion started: 8 September 2025

Unexpectedly, the σ values calculated in this study using Mie theory were significantly lower than those reported in (Zhang et al., 2023), where a two-stream radiative transfer equation was employed. The latter approach yielded relatively constant σ values and concluded that variations in K_d across the ice column were primarily driven by changes in scattering direction. The reason for this discrepancy remains unclear. However, our findings further suggest that the dominant mechanisms driving K_d variability with T_{ice} differ by depth: in surface layers, changes in the scattering direction of air bubbles prevail, whereas in deeper layers, variations in scattering magnitude due to brine inclusions play a more significant role.

4.3 Driving factors of the wavelength-dependent variations in $K_d(\lambda)$ with T_{ice}

The observed variations in K_d with T_{ice} exhibited wavelength dependence especially in the shortwave range for cold laboratory experiment. To identify the driving mechanisms behind this phenomenon, the effects of changes in V_{ice} and V_{brine} on the $a_{total}(\lambda)$ were quantitatively assessed. This is because the wavelength dependence of the K_d spectra depends mainly on the absorption properties, and the absorption coefficient of sea ice is dominated by two components, brine and pure ice. The results show that the influence of V_{ice} and V_{brine} on a_{total} was relatively minor and more evident at longer wavelengths. For example, in the upper ice layer, when T_{ice} increased from -4.8 ℃ to -1.8 ℃, $a_{total}(488)$ and $a_{total}(667)$ decreased by 0.26% and 1.65%, respectively. Similarly, in the lower ice layer, as T_{ice} rose from -4.6℃ to -2℃, $a_{total}(488)$ and $a_{total}(667)$ decreased by 0.25% and 3%, respectively. These findings indicate that temperature-induced changes in V_{ice} and V_{brine} are not the primary contributors to the wavelength-dependent behavior of K_d.

Instead, the dominant factors are likely the temperature-driven variations in $a_p(\lambda)$ and $a_{CDOM}(\lambda)$. This inference is further supported by the observation that the wavelength dependence of K_d with T_{ice} was more pronounced in the lower layers of Liaodong Bay sea ice compared to the upper layers (Figs. 5-7). The enhanced wavelength sensitivity in the lower layers is plausibly linked to higher V_{brine} and increased vertical brine porosity in the mid- and bottom-ice layers (Salomon et al., 2022), which together facilitate intra-ice brine movement. This brine flow serves as the primary transport pathway for CDOM and particulate matter, thereby amplifying the effects of a_p and a_{CDOM} on K_d. The enhanced brine connectivity allows for more dynamic redistribution of optically active substances, which contributes to the stronger wavelength dependence observed in these layers.

4.4 Limitations and implications

The analysis of the driving factors from a microstructural perspective was based on variations in V_{air} and V_{brine}, which were derived from temperature, salinity, and density measurements. However, several factors may comprise the accuracy of these parameters, particularly due to the highly dynamic environmental conditions at the sampling sites. One primary limitation arises from the influence of tidal cycles on salinity and density measurements. Since the ice cores were obtained in nearshore areas, sea ice freeboard fluctuated throughout the day in response to tidal changes. These fluctuations led to variable brine dynamics—brine infiltration during high tide and substantial brine drainage during low tide (Xu et al., 2012b). Additionally,

https://doi.org/10.5194/egusphere-2025-2373
Preprint. Discussion started: 8 September 2025

brine loss during the sampling process further introduced uncertainties in the measured salinity and density, subsequently affecting the derived estimates of V_{brine}. Another source of uncertainty stems from the spatial heterogeneity of the sea ice. The variation trends of V_{air} and V_{brine} with T_{ice} were evaluated across multiple ice samples. Although the samples were collected within a 5-meter radius, differences in physical and optical properties among them were inevitable. This heterogeneity is especially pronounced in Liaodong Bay, where sea ice conditions are influenced not only by natural variability but also by anthropogenic factors such as nearby oil-processing infrastructure and aquaculture operations.

Furthermore, the study did not directly measure the perimeters of individual inclusions, making it difficult to distinguish between brine pockets and air bubbles. As a result, all inclusions were assumed to be spherical when calculating the scattering coefficient. This simplification may underestimate the overall scattering effects, as brine inclusions are typically elongated in the vertical direction and deviate from ideal spherical geometry in their optical behavior.

While a previous study focusing on the entire ice column demonstrated a significant negative correlation between K_d and T_{ice} for young sea ice (Zhang et al., 2023), the current study reveals a more complex set of mechanisms. The relationship between K_d and T_{ice} exhibits clear depth and wavelength dependence, emphasizing the need for layer-specific analysis. Additionally, this study was limited to T_{ice} below –1.2 °C, as higher-temperature conditions correspond to "rotten" sea ice, in which the optical effects of temperature are difficult to isolate or interpret reliably. Moreover, the sea ice remained frozen throughout our measurements and did not undergo a complete freeze–thaw cycle.

It is also important to note that T_{ice} was not the sole factor influencing changes in K_d. In field observations, variations in incident shortwave radiation significantly contributed to the observed patterns. Moreover, the microstructural properties of sea ice are not governed solely by the current thermal state but are also shaped by the meteorological and hydrological conditions during the ice formation stage. To advance understanding of the processes that govern optical variability in sea ice, future research should incorporate simultaneous, high-resolution and longer-time-series measurements of ice temperature, microstructure, and downward spectral irradiance profiles across a broader temperature range, encompassing both colder and warmer regimes. Such integrative observations will help elucidate the coupled effects of thermodynamic evolution and optical behavior in natural sea ice environments.

5. Conclusion

This study aimed to investigate the characteristics and driving mechanisms underlying the variations of $K_d(\lambda)$ with T_{ice} across different depths and wavelengths, based on synchronous observations conducted in controlled laboratory settings and Liaodong Bay. The results revealed distinct depth-dependent patterns in the relationship between $K_d(\lambda)$ and T_{ice}. In the surface layer, $K_d(\lambda)$ and T_{ice} exhibited a predominantly negative correlation, occurring in 95.96% of cases. In contrast, the bottom layer showed a positive correlation in 38.38% of cases. No consistent wavelength-dependent trend was observed. Some data showed that the linear regression slopes between $K_d(\lambda)$ and T_{ice} were most pronounced in the blue-green band range (443–555 nm), while most data showed minimal variations across the visible spectrum. Further analysis of the

https://doi.org/10.5194/egusphere-2025-2373
Preprint. Discussion started: 8 September 2025

microstructural and optical properties suggested that the observed variations in $K_d(\lambda)$ with T_{ice} were primarily driven by changes in V_{air} in the surface layers and V_{brine} in the bottom layers. Additionally, the transport of particulate matter and CDOM within brine channels may explain the occasional wavelength dependence in the shortwave region. This study advances our understanding of the temperature sensitivity of sea ice light attenuation and highlights the need for further research. Future efforts should aim to incorporate a broader set of environmental variables, such as incident shortwave and longwave radiation, and to investigate $K_d(\lambda)$ behaviour during the complete freezing–thawing cycles

Data availability. Data are available upon request.

Author contributions. YZ and ZX conceived and conducted the laboratory and field studies. YZ processed and analyzed the data, and wrote the paper. All co-authors discussed the results and edited the manuscript.

Competing interests. The contact author has declared that none of the authors has any competing interests.

Disclaimer. Publisher's note: Copernicus Publications remains neutral with regard to jurisdictional claims in published maps and institutional affiliations.

Acknowledgements. We wish to express our appreciation to colleagues in the Optics Laboratory at the South China Sea Institute of Oceanology, Chinese Academy of Sciences, who contributed to the sea ice field surveys in Liaodong Bay. We are also grateful for the help provided by the Polar Ice Science and Engineering research team of Dalian University of Technology.

Financial support. This research was supported by the National Natural Science Foundation of China (NSFC) (42076190, 41776044), the National Science & Technology Fundamental Resources Investigation Program of China (2018FY100100), the Basic and applied basic Research Foundation of Guangdong Province (2021A1515011538), the Key Deployment Project of Centre for Ocean Mega-Research of Science, Chinese Academy of Science (COMS2019J10), and the China Postdoctoral Science Foundation under Grant Number 2024M762121. We wish to express our appreciation to our colleagues in the South China Sea Institute of Oceanology, Chinese Academy of Sciences, who contributed to the sea ice field surveys in Liaodong Bay.

References

Arndt, S. and Nicolaus, M.: Seasonal cycle and long-term trend of solar energy fluxes through Arctic sea ice, Cryosphere, 8, 2219-2233, 10.5194/tc-8-2219-2014, 2014.

https://doi.org/10.5194/egusphere-2025-2373
Preprint. Discussion started: 8 September 2025

Comiso, J. C., Parkinson, C. L., Gersten, R., and Stock, L.: Accelerated decline in the Arctic Sea ice cover, Geophysical Research Letters, 35, 6, 10.1029/2007gl031972, 2008.

Cox, G. F. N. and Weeks, W. F.: Equations for Determining the Gas and Brine Volumes in Sea-ice Samples, Journal of Glaciology, 29, 306-316, 10.3189/s0022143000008364, 1983.

Crabeck, O., Galley, R. J., Mercury, L., Delille, B., Tison, J. L., and Rysgaard, S.: Evidence of Freezing Pressure in Sea Ice Discrete Brine Inclusions and Its Impact on Aqueous-Gaseous Equilibrium, J. Geophys. Res.-Oceans, 124, 1660-1678, 10.1029/2018jc014597, 2019.

Curry, J. A., Schramm, J. L., and Ebert, E. E.: Sea Ice-Albedo Climate Feedback Mechanism, Journal of Climate, 8, 240-247, 1995.

Dash, J. G., Rempel, A. W., and Wettlaufer, J. S.: The physics of premelted ice and its geophysical consequences, Reviews of Modern Physics, 78, 695-741, 10.1103/RevModPhys.78.695, 2006.

Ebert, E. E., Schramm, J. L., and Curry, J. A.: Disposition of Solar-radiation in Sea-ice and the Upper Ocean, J. Geophys. Res.-Oceans, 100, 15965-15975, 10.1029/95jc01672, 1995.

Ehn, J. K., Papakyriakou, T. N., and Barber, D. G.: Inference of optical properties from radiation profiles within melting landfast sea ice, J. Geophys. Res.-Oceans, 113, 15, 10.1029/2007jc004656, 2008.

Ehn, J. K., Hwang, B. J., Galley, R., and Barber, D. G.: Investigations of newly formed sea ice in the Cape Bathurst polynya: 1. Structural, physical, and optical properties, J. Geophys. Res.-Oceans, 112, 15, 10.1029/2006jc003702, 2007.

Erickson, D. D.: The optical properties of sea ice: Temperature, salinity, and wavelength dependence, Univ. of Wash., Seattle, 2002.

Frantz, C. M., Light, B., Farley, S. M., Carpenter, S., Lieblappen, R., Courville, Z., Orellana, M. V., and Junge, K.: Physical and optical characteristics of heavily melted "rotten" Arctic sea ice, Cryosphere, 13, 775-793, 10.5194/tc-13-775-2019, 2019.

Graversen, R. G., Mauritsen, T., Tjernstrom, M., Kallen, E., and Svensson, G.: Vertical structure of recent Arctic warming, Nature, 451, 53-U54, 10.1038/nature06502, 2008.

Grenfell, T. C.: A theoretical model of the optical properties of sea ice in the visible and near infrared, J. Geophys. Res, 88, 1983.

Grenfell, T. C. and Perovich, D. K.: Radiation absorption-coefficients of polycrystalline ice from 400-1400 nm, J. Geophys. Res.-Oceans, 86, 7447-7450, 10.1029/JC086iC08p07447, 1981.

Grenfell, T. C., Light, B., and Perovich, D. K.: Spectral transmission and implications for the partitioning of shortwave radiation in arctic sea ice, Annals of Glaciology, Vol 44, 2006, 44, 1-+, 10.3189/172756406781811763, 2006.

Hall, A.: The role of surface albedo feedback in climate, Journal of Climate, 17, 1550-1568, 10.1175/1520-0442(2004)017<1550:trosaf>2.0.co;2, 2004.

Ingram, W. J., Wilson, C. A., and Mitchell, J. F. B.: Modeling Climate Change - An Assessment of Sea Ice and Surface Albedo Feedbacks J. Geophys. Res.-Atmos., 94, 8609-8622, 10.1029/JD094iD06p08609, 1989.

https://doi.org/10.5194/egusphere-2025-2373
Preprint. Discussion started: 8 September 2025

Kauko, H. M., Taskjelle, T., Assmy, P., Pavlov, A. K., Mundy, C. J., Duarte, P., Fernandez-Mendez, M., Olsen, L. M., Hudson, S. R., Johnsen, G., Elliott, A., Wang, F. Y., and Granskog, M. A.: Windows in Arctic sea ice: Light transmission and ice algae in a refrozen lead, Journal of Geophysical Research-Biogeosciences, 122, 1486-1505, 10.1002/2016jg003626, 2017.

Light, B., Maykut, G. A., and Grenfell, T. C.: Effects of temperature on the microstructure of first-year Arctic sea ice, Journal of Geophysical Research Oceans, 108, -, 2003a.

Light, B., Maykut, G. A., and Grenfell, T. C.: A two-dimensional Monte Carlo model of radiative transfer in sea ice, J. Geophys. Res.-Oceans, 108, 18, 10.1029/2002jc001513, 2003b.

Light, B., Maykut, G. A., and Grenfell, T. C.: A temperature-dependent, structural-optical model of first-year sea ice, J. Geophys. Res.-Oceans, 109, 19, 10.1029/2003jc002164, 2004.

Light, B., Perovich, D. K., Webster, M. A., Polashenski, C., and Dadic, R.: Optical properties of melting first-year Arctic sea ice, J. Geophys. Res.-Oceans, 120, 7657-7675, 10.1002/2015jc011163, 2015.

Macfarlane, A. R., Dadic, R., Smith, M. M., Light, B., Nicolaus, M., Henna-Reetta, H., Webster, M., Linhardt, F., Hämmerle, S., and Schneebeli, M.: Evolution of the microstructure and reflectance of the surface scattering layer on melting, level Arctic sea ice, Elementa-Sci. Anthrop., 11, 10.1525/elementa.2022.00103, 2023.

Marks, A. A., Lamare, M. L., and King, M. D.: Optical properties of sea ice doped with black carbon - an experimental and radiative-transfer modelling comparison, Cryosphere, 11, 2867-2881, 10.5194/tc-11-2867-2017, 2017.

Nicolaus, M., Katlein, C., Maslanik, J., and Hendricks, S.: Changes in Arctic sea ice result in increasing light transmittance and absorption, Geophysical Research Letters, 39, 6, 10.1029/2012gl053738, 2012.

Pegau, W. S. and Zaneveld, J. R. V.: Field measurements of in-ice radiance, Cold Regions Science and Technology, 31, 33-46, 10.1016/s0165-232x(00)00004-5, 2000.

Perovich, D., Light, B., and Dickinson, S.: Changing ice and changing light: trends in solar heat input to the upper Arctic ocean from 1988 to 2014, Annals of Glaciology, 61, 401-407, 10.1017/aog.2020.62, 2020.

Perovich, D. K.: On the aggregate-scale partitioning of solar radiation in Arctic sea ice during the Surface Heat Budget of the Arctic Ocean (SHEBA) field experiment, J. Geophys. Res.-Oceans, 110, 12, 10.1029/2004jc002512, 2005.

Perovich, D. K.: Sea ice and sunlight, Sea Ice2017.

Perovich, D. K. and Grenfell, T. C.: Laboratory Studies of the Optical - Properties of Young Sea Ice, Journal of Glaciology, 27, 331-346, 10.3189/s0022143000015410, 1981.

Perovich, D. K. and Polashenski, C.: Albedo evolution of seasonal Arctic sea ice, Geophysical Research Letters, 39, 6, 10.1029/2012gl051432, 2012.

Perovich, D. K., Jones, K. F., Light, B., Eicken, H., Markus, T., Stroeve, J., and Lindsay, R.: Solar partitioning in a changing Arctic sea-ice cover, Annals of Glaciology, 52, 192-196, 10.3189/172756411795931543, 2011.

Salomon, M. L., Maus, S., and Petrich, C.: Microstructure evolution of young sea ice from a Svalbard fjord using micro-CT analysis, Journal of Glaciology, 68, 571-590, 10.1017/jog.2021.119, 2022.

https://doi.org/10.5194/egusphere-2025-2373
Preprint. Discussion started: 8 September 2025

Serreze, M. C., Holland, M. M., and Stroeve, J.: Perspectives on the Arctic's shrinking sea-ice cover, Science, 315, 1533-1536, 10.1126/science.1139426, 2007.

Smith, R. C. and Baker, K. S.: Optical-properties of the clearest natural-waters (200-800 nm), Applied Optics, 20, 177-184, 10.1364/ao.20.000177, 1981.

Taskjelle, T., Hudson, S. R., Granskog, M. A., Nicolaus, M., Lei, R. B., Gerland, S., Stamnes, J. J., and Hamre, B.: Spectral albedo and transmittance of thin young Arctic sea ice, J. Geophys. Res.-Oceans, 121, 540-553, 10.1002/2015jc011254, 2016.

Thomas, M., France, J., Crabeck, O., Hall, B., Hof, V., Notz, D., Rampai, T., Riemenschneider, L., Tooth, O. J., Tranter, M., and Kaiser, J.: The Roland von Glasow Air-Sea-Ice Chamber (RvG-ASIC): an experimental facility for studying ocean-sea-ice-atmosphere interactions, Atmos. Meas. Tech., 14, 1833-1849, 10.5194/amt-14-1833-2021, 2021.

Van de Hulst, H. C.: Multiple Light Scattering Tables, Formulas, and Applications,, San Diego, Calif., University of California, San Diego, 739 pp., 1980.

Wang, Q., Lu, P., Lepparanta, M., Cheng, B., Zhang, G., and Li, Z.: Physical Properties of Summer Sea Ice in the Pacific Sector of the Arctic During 2008-2018, J. Geophys. Res.-Oceans, 125, 10.1029/2020jc016371, 2020.

Xu, Z., Yang, Y., Sun, Z., Li, Z., Cao, W., and Ye, H.: In situ measurement of the solar radiance distribution within sea ice in Liaodong Bay, China, Cold Regions Science and Technology, 71, 23-33, 10.1016/j.coldregions.2011.10.005, 2012a.

Xu, Z., Yang, Y., Wang, G., Cao, W., Li, Z., and Sun, Z.: Optical properties of sea ice in Liaodong Bay, China, Journal of Geophysical Research: Oceans, 117, n/a-n/a, 10.1029/2010jc006756, 2012b.

Yu, M., Lu, P., Cheng, B., Leppaeranta, M., and Li, Z. J.: Impact of Microstructure on Solar Radiation Transfer Within Sea Ice During Summer in the Arctic: A Model Sensitivity Study, Front. Mar. Sci., 9, 10.3389/fmars.2022.861994, 2022.

Yu, M., Lu, P., Leppäranta, M., Cheng, B., Lei, R., Li, B., Wang, Q., and Li, Z.: Modeled variations in the inherent optical properties of summer Arctic ice and their effects on the radiation budget: a case based on ice cores from 2008 to 2016, The Cryosphere, 18, 273-288, 10.5194/tc-18-273-2024, 2024.

Zhang, Y., Xu, Z. T., Ehn, J. K., Diaz, A., and Yang, Y. Z.: A significant change in sea ice diffuse attenuation coefficient with temperature and its implications for the Arctic Ocean, Limnol. Oceanogr., 68, 2431-2444, 10.1002/lno.12432, 2023.

Zhao, J. P., Li, T., Barber, D., Ren, J. P., Pucko, M., Li, S. J., and Li, X.: Attenuation of lateral propagating light in sea ice measured with an artificial lamp in winter Arctic, Cold Regions Science and Technology, 61, 6-12, 10.1016/j.coldregions.2009.12.006, 2010.